Physical and Soluble Cues Enhance Tendon Progenitor Cell Invasion into Injectable Synthetic Hydrogels

Robert N. Kent III, Mohamed Said, Megan E. Busch, Ethan R. Poupard, Ariane Tsai, Jingyi Xia, Daniel L. Matera, William Y. Wang, Samuel J. DePalma, Harrison L. Hiraki, Megan L. Killian, Adam C. Abraham, Jae-Won Shin, Alice H. Huang, Ariella Shikanov, and Brendon M. Baker*

Synthetic hydrogels represent an exciting avenue in the field of regenerative bio-materials given their injectability, orthogonally tunable mechanical properties, and potential for modular inclusion of cellular cues. Separately, recent advances in soluble factor release technology have facilitated control over the soluble milieu in cell microenvironments via tunable microparticles. A composite hydrogel incorporating both of these components can robustly mediate tendon healing following a single injection. Here, a synthetic hydrogel system with encapsulated electrospun fiber segments and a novel microgel-based soluble factor delivery system achieves precise control over topographical and soluble features of an engineered microenvironment, respectively. It is demonstrated that three-dimensional migration of tendon progenitor cells can be enhanced via combined mechanical, topographical, and microparticle-delivered soluble cues in both a tendon progenitor cell spheroid model and an ex vivo murine Achilles tendon model. These results indicate that fiber reinforced hydrogels can drive the recruitment of endogenous progenitor cells relevant to the regeneration of tendon and, likely, a broad range of connective tissues.

1. Introduction

In the USA, 124 million cases of musculoskeletal injury are reported annually, with an overall financial burden exceeding $100 billion per year.[1] Tendon and ligament injuries comprise an estimated 45% of these cases.[2] In particular, the Achilles tendon (AT) is one of the most commonly injured (≈30 000 cases annually) given its enormous mechanical demands, especially during sports activity.[3] Current treatment options for AT rupture include surgical approximation of the tendon stubs or the conservative route of temporary immobilization and rehabilitation; unfortunately, both treatment options end in comparably poor patient outcomes with regard to functional restoration, return to pre-injury levels of activity, chronic pain, and heightened risk of reinjury.[4] These poor outcomes are largely attributed to the generation of disorganized, hypervascularized, hypercellular scar tissue lacking the architecture and mechanical properties necessary to meet the functional demands of the tendon.[5] Thus, restoration of native tendon composition and architecture following AT rupture would dramatically improve patient outcomes and reduce the significant economic burden of these injuries.[6]

Despite possessing a population of tendon progenitor cells (TPCs) in the epitenon, injured tendons fail to recruit or properly differentiate these progenitors.[7] Therefore, therapies that can influence the identity and quantity of repair cells recruited to the injury site are likely required for the regeneration of functional tendon in lieu of dysfunctional scar tissue. While injection and suture-based delivery of drugs and biologics such

---

R. N. Kent III, M. Said, M. E. Busch, E. R. Poupard, A. Tsai, J. Xia,
D. L. Matera, W. Y. Wang, S. J. DePalma, H. L. Hiraki,
A. Shikanov, B. M. Baker
Department of Biomedical Engineering
University of Michigan
2174 Lurie BME Building, 1101 Beal Avenue, Ann Arbor, MI 48109, USA
E-mail: bambren@umich.edu

M. L. Killian, A. C. Abraham
Department of Orthopedic Surgery
University of Michigan
Ann Arbor, MI 48109, USA

J.-W. Shin
Department of Pharmacology and Regenerative Medicine, Department of Biomedical Engineering
University of Illinois Chicago
Chicago, IL 60607, USA

A. H. Huang
Department of Orthopedic Surgery
Columbia University
New York, NY 10032, USA

B. M. Baker
Department of Chemical Engineering
University of Michigan
Ann Arbor, MI 48109, USA

as growth factors, platelet-rich plasma, and stem cells, have shown some promise, these approaches lack the spatiotemporal control required for regenerating the tendon's native architecture.[8] To address this problem, efforts have shifted toward tissue constructs engineered to recapitulate the biomechanical and topographical properties of tendon. However, even with aligned topography, materials whose tensile moduli approach that of native tendon can promote aberrant differentiation of progenitors toward chondrogenic or osteogenic lineages.[9]

Synthetic hydrogels represent an exciting approach to tissue repair-mediating biomaterials that can be localized to an internal wound defect through minimally invasive administration. Typically composed of polymer chains cross-linked into a solid bulk by protease-cleavable peptides, these materials also benefit from tunable and modular inclusion of biochemical moieties in addition to tailorable mechanical properties.[10] However, optimizing physical cues to permit cell infiltration while still maintaining the mechanical properties required for a musculoskeletal implant remains challenging.[11] Analogous to rebar-reinforced concrete, synthetic fibers can mechanically reinforce hydrogels by increasing their tensile strength with the added benefit of providing topographical cues that guide 3D cell migration and spreading.[10,11b,12] Separately, recent advances in soluble factor release technology have demonstrated heparin microparticle-mediated, sustained release of growth factors. Through affinity interactions that reversibly bind and stabilize growth factors and chemokines, heparin-based particles circumvent the issue of burst release associated with typical microparticle-based delivery systems.[13] Together, these developments suggest that a composite hydrogel incorporating tunable fibrous topography and soluble factor delivery could mediate tendon regeneration with a single injection.

Here, we developed a synthetic mimic of the provisional matrix that forms shortly after AT rupture to assess whether the recruitment of tendon progenitor cells (TPCs) can be enhanced via combined mechanical, topographical, and microparticle-delivered soluble cues. We formed hydrogels from vinyl sulfonated dextran (DexVS) cross-linked with an MMP-labile peptide and imbued this microenvironment with topographical cues by incorporating electrospun DexVS fiber segments.[10] This material approach facilitated orthogonal tuning of fibrous topography and bulk mechanics, both of which influence TPC invasion. Monodisperse populations of hybrid DexVS microgels with covalently incorporated heparin were then fabricated to release PDGF-BB, a chemokine that potently induces TPC migration. Using this material platform, we found that recruitment of murine TPCs into DexVS hydrogels was enhanced by fibrous topographical cues and microgel-delivered PDGF-BB. These cues translated effectively to an ex vivo model of TPC recruitment from the epitenon of explanted murine ATs.

2. Results and Discussion

2.1. PDGF-BB Drives TPC Invasion into DexVS Hydrogels

For efficient screening of microenvironmental conditions that promote TPC recruitment, we chose a spheroid model given its throughput and clear demarcation of initial cell positions

relative to final positions following cellular outgrowth.[14] Previous work has explored the role of various chemokines on the recruitment of TPCs during development and healing in vivo in addition to scratch and transwell migration assays in vitro.[9c,15] Using this prior work as a starting point, we tested a panel of known chemokines comprised of transforming growth factor (TGF)-β1, stromal cell-derived factor (SDF)-1α, and platelet-derived growth factor (PDGF)-BB for their ability to recruit TPCs into synthetic, cell-degradable DexVS/VPMS hydrogels (**Figure 1**A). A range of doses (media supplemented with 10–100 ng mL^{-1}) was tested for each chemokine. Independent of dose, PDGF-BB was the only soluble cue capable of driving 3D TPC invasion into synthetic hydrogel matrices, as evidenced by increased outgrowth area, number of migrating cells, and total migration distance (Figure 1B–E). This result was unexpected given the range of contexts in which TGF-β1 and SDF-1α have previously been shown to promote TPC recruitment.[9c,15b] Previous work has implicated increased matrix metalloproteinase (MMP) production, which facilitates extracellular matrix (ECM) degradation, in the mechanism of PDGF-induced cell migration.[16] Therefore, our observation that solely PDGF-BB induces TPC migration into MMP-cleavable DexVS/VPMS hydrogels may stem from the nanoporosity of these materials,[10] which may necessitate matrix proteolysis and cytoskeletal remodeling distinct from the requirements for migration in 2D or in vivo settings.[17]

Since PDGF-BB has previously been demonstrated to act as both a chemokine and a mitogen,[18] we next investigated the extent to which these two distinct cell functions contributed to TPC outgrowth from spheroids in synthetic hydrogels. A higher proportion of cells were positive for Ki67 immunostaining with PDGF-BB treatment compared to vehicle controls (Figure 1F,G), indicating that PDGF-BB-mediated proliferation may contribute to the increased number of invading cells. To confirm the role of proliferation in PDGF-BB-driven cell invasion, cell division was pharmacologically blocked by mitomycin C treatment prior to spheroid formation and encapsulation. Strikingly, inhibiting cell proliferation completely abrogated enhanced outgrowth in response to PDGF-BB (Figure S1, Supporting Information). Taken together, these results indicate that PDGF-BB-induced proliferation is a key component of TPC outgrowth into synthetic hydrogels, challenging the classical paradigm that cell migration and proliferation represent mutually exclusive cell functions.[19]

2.2. Fibrous Topography Enhances PDGF-BB-Driven TPC Invasion

Nanoporous synthetic hydrogels can support cell migration and are ideal for minimally invasive therapeutic administration via injection. However, in contrast to native ECM, these amorphous materials lack cell-scale fibrous topography, which is known to impact cell spreading and migration.[10,21] Therefore, we explored the effect of incorporating synthetic, cell-adhesive fibers on TPC spheroid outgrowth in a DexVS hydrogel. DexVS fiber segments were electrospun and functionalized with RGD to enable cell adhesion required for contact guided migration (**Figure 2**A). The surrounding DVS bulk

ADVANCED
SCIENCE NEWS
www.advancedsciencenews.com

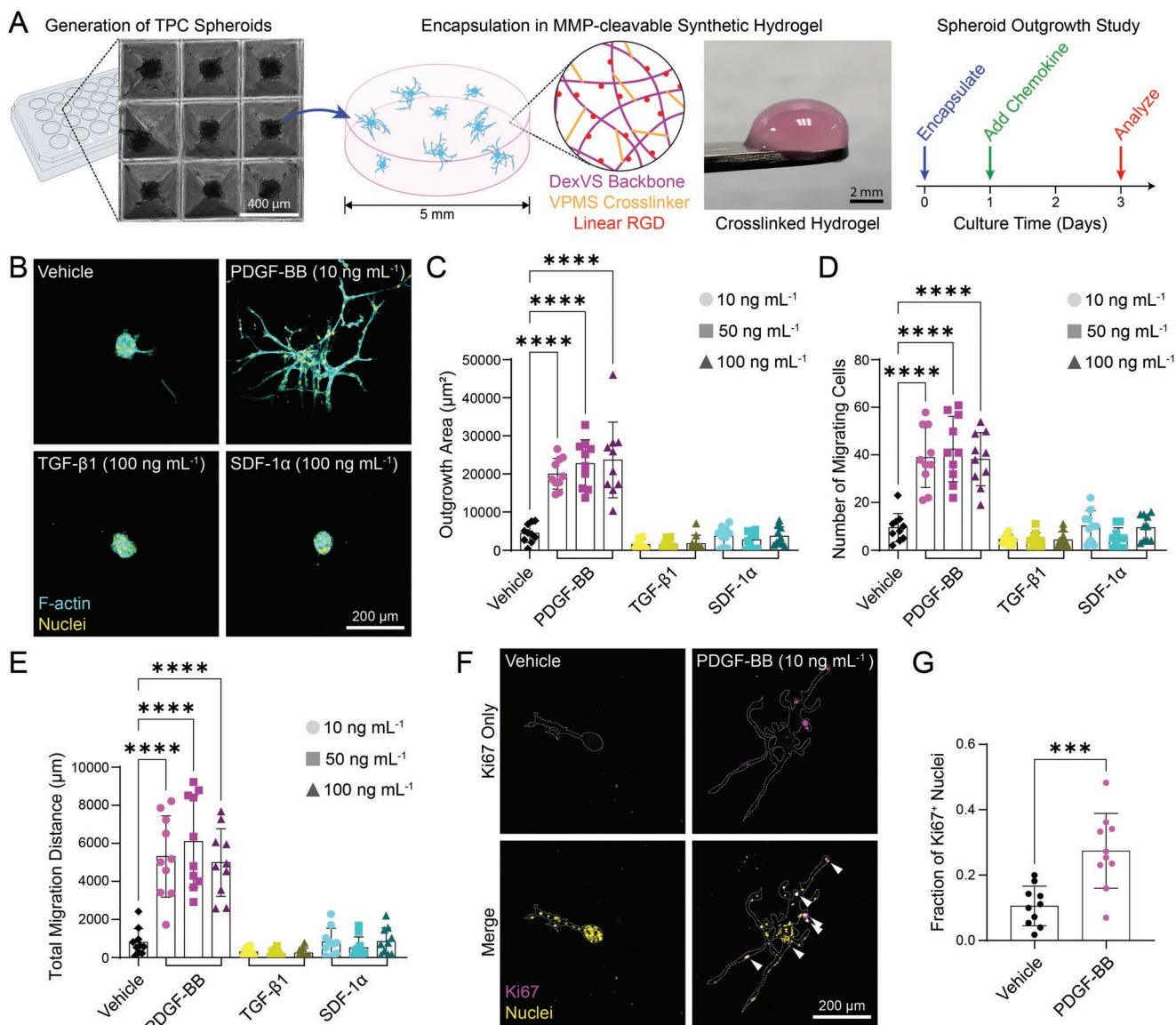ADVANCED
FUNCTIONAL
MATERIALS
www.afm-journal.de

Figure 1. PDGF-BB enhances TPC invasion into synthetic hydrogels. A) Experimental schematic; TPC spheroids were encapsulated in a 0.5 kPa DexVS/VPMS hydrogel,[20] and outgrowth proceeded for 3 days before fixation, with chemokine supplementation on day 1. B) Confocal fluorescent images of spheroid outgrowth, varying chemokine identity and concentration. Quantification of C) spheroid outgrowth area (μm^2), D) number of migrating cells, and E) total migration distance (μm) ($n = 10$ spheroids, $N = 2$). F) Confocal fluorescent images of spheroids stained for Ki67, with dotted white lines delineating cytoplasmic boundaries. White arrowheads indicate Ki67$^+$ nuclei in the merged panels. G) Quantification of the fraction of Ki67$^+$ nuclei ($n = 10$). All data are presented as mean ± standard deviation. Asterisks indicate statistically significant comparisons, with $^{***}p < 0.001$ and $^{****}p < 0.0001$ by ordinary one-way ANOVA with Tukey's multiple comparisons test or Student's t-test.

hydrogel was also functionalized with RGD to allow TPCs to adhere, spread, and migrate independently of additional fibrous guidance queues. In the presence of 10 ng mL^{-1} PDGF-BB, inclusion of cell-adhesive fibers led to marked increases in cell outgrowth compared to non-fibrous controls. This result is intuitive given the well-described role of contact guidance in cell spreading and migration, where cells sense and respond to the anisotropic mechanics and topography of cell-adhesive fibrillar ECM.[22] Incorporating synthetic fiber segments provides anisotropic mechanical cues in an otherwise isotropic hydrogel, likely facilitating contact guided, 3D cell migration into the construct.[14b]

To evaluate the effect of bulk cross-linking on fiber-guided TPC migration, hydrogels were cross-linked with 12.5 or 20.0 mM VPMS to achieve bulk stiffnesses of ≈0.5 or 2.0 kPa, respectively.[20] Importantly, in contrast to those of natural hydrogels, topographical cues in this system can be tuned independently of bulk mechanical properties.[10,20] While increasing cross-linking density led to a general attenuation in migration, outgrowth in more densely cross-linked (20 mM VPMS) gels was partially rescued at the highest fiber density tested (Figure 2B–E). These results suggest that a minimum threshold of fiber density may be required at a given bulk cross-linking density such that the contact guidance cues are
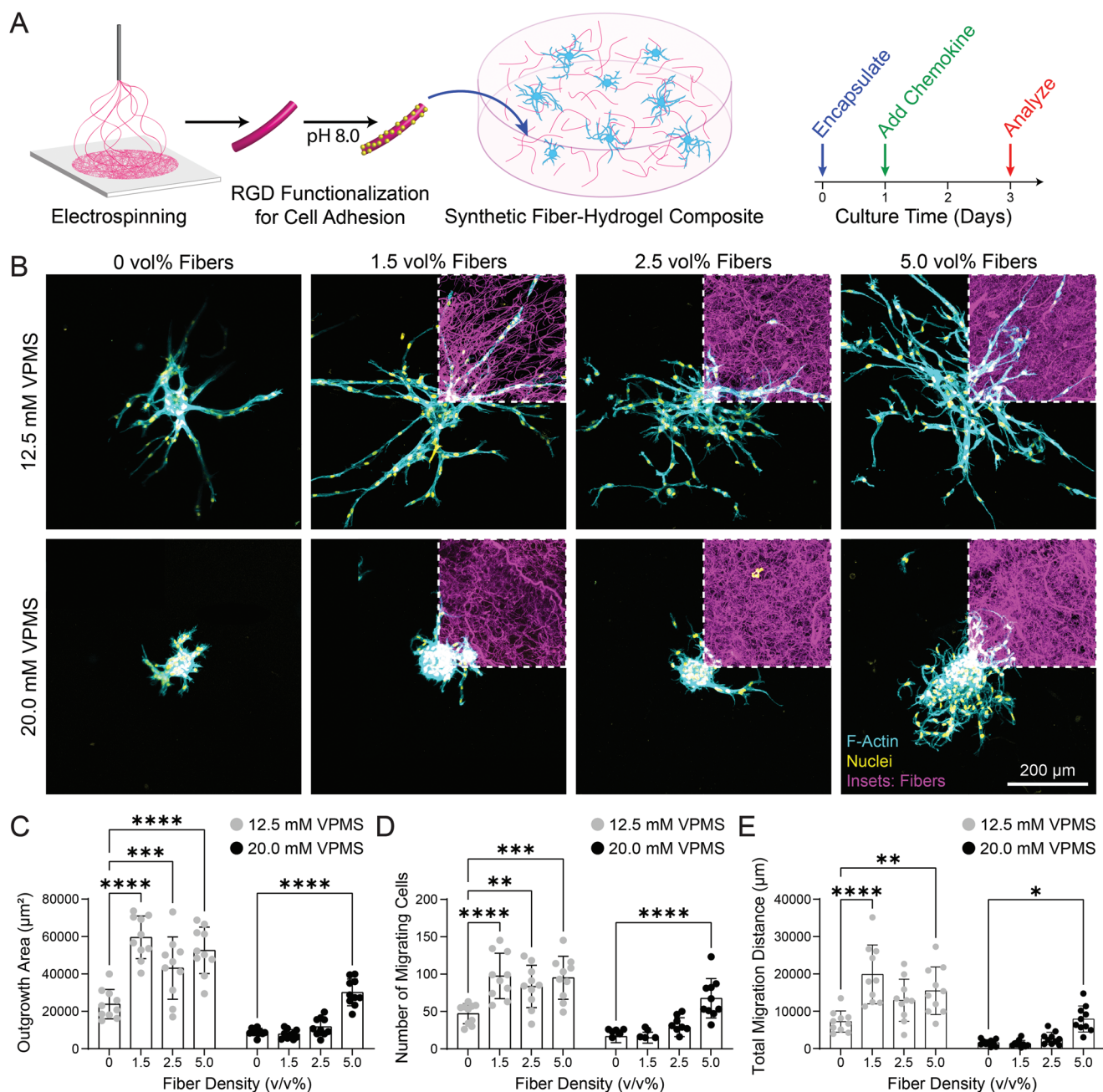
**ADVANCED
SCIENCE NEWS**

www.advancedsciencenews.com

**ADVANCED
FUNCTIONAL
MATERIALS**

www.afm-journal.de

Figure 2. Fibrous topography enhances TPC invasion. A) Experimental schematic; DexVS fibers were electrospun, functionalized with cell-adhesive RGD, and co-encapsulated with TPC spheroids in a DexVS/VPMS hydrogel; following encapsulation, all samples were supplemented with PDGF-BB on day 1, and outgrowth proceeded until fixation on day 3. B) Confocal fluorescent images of TPC spheroid outgrowth, varying fiber density and bulk stiffness. Quantification of C) TPC spheroid outgrowth area (μm^2), D) number of migrating cells, and E) total migration distance (μm) ($n = 10$, $N = 2$). All data are presented as mean ± standard deviation. Asterisks indicate statistically significant comparisons, with $^{**}p < 0.01$, $^{***}p < 0.001$, and $^{****}p < 0.0001$ by ordinary two-way ANOVA with Tukey's multiple comparisons test.

readily accessible to encapsulated cells. In the interest of eventually pursuing in vivo applications of this biomaterial system in mechanically demanding tissue spaces,[11a,21b] we screened TPC outgrowth as a function of VPMS concentration to find that 15 mM VPMS is the threshold above which migration is significantly limited in nonfibrous hydrogels (Figure S2, Supporting Information). Subsequent outgrowth studies were thus performed in bulk hydrogels crosslinked with 15 mM VPMS.

We hypothesized that removing RGD from the bulk hydrogel would maximize the capacity of topographical cues to guide cell migration, as cells would only be able to form adhesions on the encapsulated fibers. However, by repeating spheroid outgrowth studies in fibrous DexVS hydrogels with the bulk hydrogel functionalized with a scrambled sequence (CRDGS, i.e., RDG), we found that the presence or absence of adhesive moieties in the bulk hydrogel had no impact on fiber-mediated outgrowth
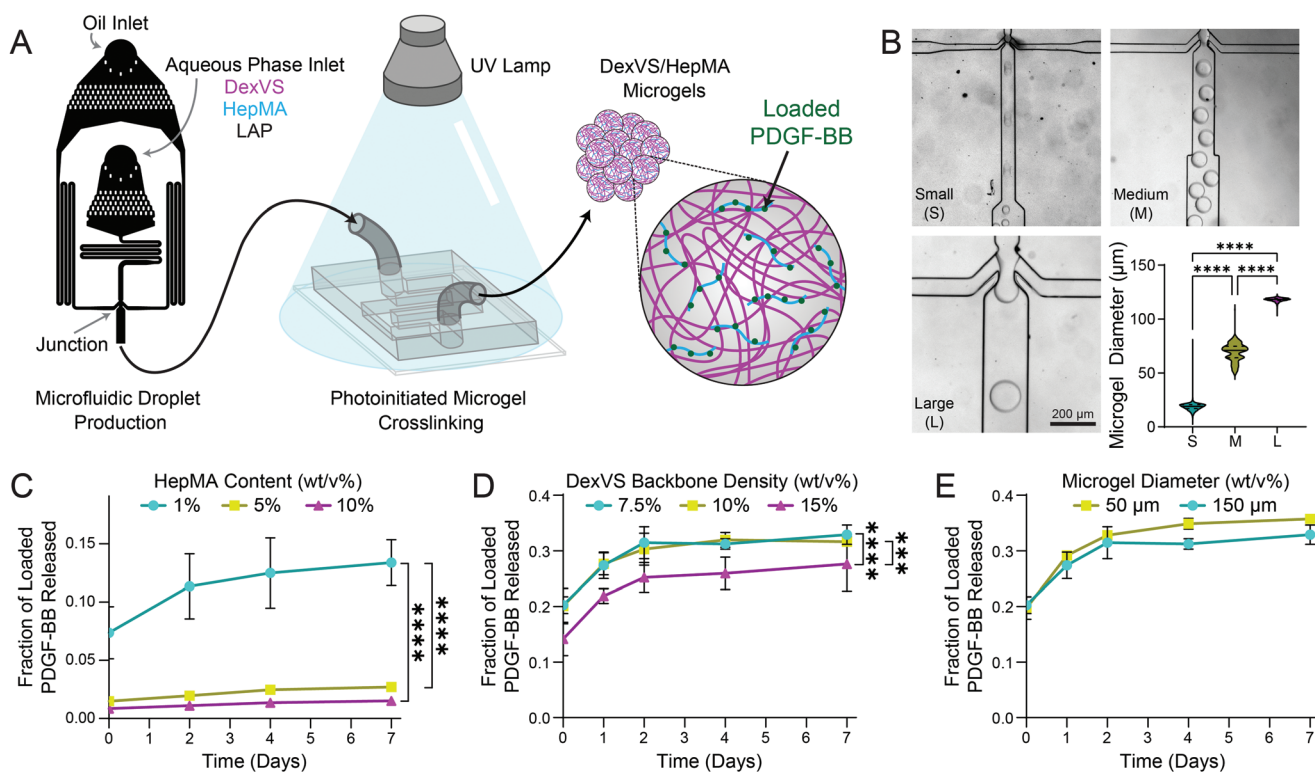
Figure 3. Heparin content dictates soluble factor release kinetics from hybrid microgels. A) AutoCAD rendering of a microfluidic device design for generating and photo-crosslinking monodisperse DexVS/HepMA microgels. B) Images of varying droplet diameter as a function of channel geometry and quantification of droplet diameters (Small $n = 13\,827$, Medium $n = 476$, Large $n = 1748$) (solid horizontal line denotes median; dashed lines denote Q1 and Q3). C) PDGF-BB released from hybrid microgels over time, varying HepMA wt/v%, D) DexVS wt/v%, and E) microgel diameter (all $n = 2$) (data presented as mean ± standard deviation). Asterisks indicate statistically significant comparisons, with [***] $p < 0.001$ and [****] $p < 0.0001$ by ordinary one-way ANOVA with Tukey's multiple comparisons test.

(Figure S3, Supporting Information). The finding that fibrous topography can promote 3D TPC migration suggests that aligned 3D topography may improve alignment of recruited TPCs[14a] and, possibly, alignment of de novo ECM.[9d,12] Thus, anticipating future work that will investigate the effects of aligned fibrous topography on cell and de novo ECM organization, we used RDG-functionalized bulk hydrogels in all subsequent outgrowth studies.

2.3. Hybrid DexVS/HepMA Microgels Enable Tunable Release of TPC Chemokines

Achieving gradual release of chemokines is paramount for eventual in vivo translation of this material system, which would ideally only involve a single transcutaneous or intraoperative administration. Having identified a chemokine that robustly mediates TPC proliferation and migration, we next incorporated PDGF-BB into microgels to mediate gradual release of this factor to drive TPC recruitment. Given that the rate of soluble factor release is theoretically dependent on microparticle geometry,[23] high-throughput generation of spherical microgels with controlled and monodisperse diameters is critical. Therefore, we fabricated microfluidic droplet-generating devices possessing defined geometries to generate spherical microgels over a range of diameters (**Figure 3**A,B).[24]

Heparin-based delivery vehicles can prolong the release of heparin-binding soluble cues in cell microenvironments, preventing the burst release associated with traditional soluble factor delivery vehicles.[13a,b] To take advantage of heparin's known affinity for a wide range of chemokines and growth factors, including PDGF-BB,[13,25] we fabricated hybrid microgels by covalently incorporating methacrylated heparin (HepMA) into DexVS microgels via photoinitiated cross-linking (Figure 3C).[26] Microgels (150 μm diameter) containing 1, 5, and 10 wt/v% HepMA were loaded at 250 ng mL^{-1} with PDGF-BB and assayed by ELISA for PDGF-BB release over the course of 1 week. HepMA incorporation led to a marked attenuation in PDGF-BB release rate (Figure 3D). Increasing DexVS weight percent above 10 wt/v% resulted in a slower release rate, likely due to decreased pore size, but this effect was small compared to that of HepMA inclusion (Figure 3E). Microgel size and chemokine loading duration showed no effect, whereas doubling the chemokine loading concentration resulted in equivalent release profiles in terms of the fraction of loaded PDGF-BB, enabling facile control over the absolute mass of delivered payload (Figure S4, Supporting Information). Together, these results demonstrate that affinity interactions between sulfate-rich heparin and positively charged PDGF-BB dictate the rate of release, rather than the steric hindrance traditionally associated with drug-delivering biomaterials.[27] Importantly, this delivery vehicle can be employed for a wide range of soluble
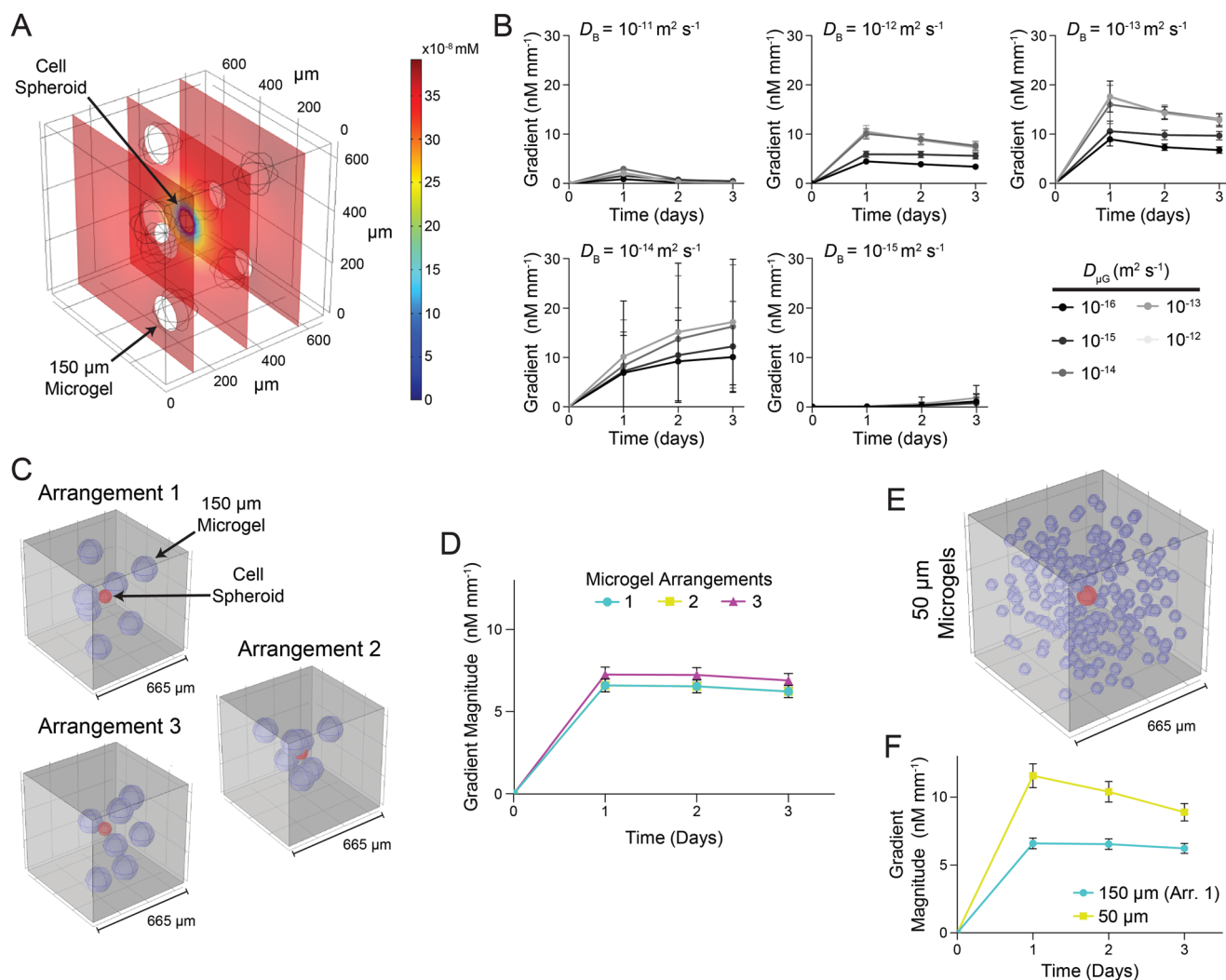
Figure 4. Computational model predicts release kinetics from hydrogel-encapsulated microgels. A) Rendering of spatial distribution of chemokine (150 µm microgels incorporated at 2.5 $v/v\%$) on day 3, with bulk (D_B) and microgel ($D_{\mu G}$) diffusion coefficients set to 10^{-12} and 10^{-15} m^2 s^{-1}. B) Gradient of chemokine concentration (nм mm^{-1}) over the first 20 microns adjacent to the TPC spheroid boundary across a range of D_B and $D_{\mu G}$ over a 3 day period. C) Renderings of model geometries with the microgel distribution in (A) and (B) (Arrangement 1) and two additional random arrangements, with cell spheroids shown in red and hybrid microgels shown in blue. D) Gradient quantification of arrangements in (C). E) Rendering of model geometry with 50 µm microgels incorporated at 2.5 $v/v\%$. F) Gradient magnitude of the model in (E) compared to Arrangement 1 from (C). All data are presented as mean ± standard deviation. $n = 6$ radial directions for all gradient measurements.

factors to drive chemotaxis, differentiation, or immunomodulation so long as they carry a positive charge in physiologic conditions.[13,25]

2.4. Computational Modeling Predicts Microgel-Mediated Delivery of Chemokines by Hybrid Microgels

To better understand chemokine release kinetics from hybrid microgels encapsulated in a bulk hydrogel, we developed a model in COMSOL representing a 10x field of view centered on a cell spheroid with surrounding microgels incorporated at a density of 2.5 v/v% (**Figure** 4A). Varying the fluid diffusion coefficient of microgels ($D_{\mu G}$) as a surrogate for HepMA content, with lower $D_{\mu G}$ values reflecting higher HepMA concentration,

we first explored the effect of $D_{\mu G}$ and the diffusion coefficient of the bulk hydrogel (D_B) on the formation of chemokine concentration gradients adjacent to the cell spheroid. This screen suggests that varying HepMA concentration can impact chemokine gradients over three days, but only within a D_B range of 10^{-12}–10^{-14} m^2 s^{-1} (Figure 4B). Previous work has measured the diffusion coefficient of DexVS/VPMS hydrogels from 10^{-16} to 10^{-15} m^2 s^{-1}, but these values were determined by diffusion of fluorescent dextran.[28] Given that PDGF-BB is a globular protein (and not a linear polysaccharide), we expect D_B here to be above this range. For all subsequent perturbations, we set D_B and $D_{\mu G}$ to 10^{-12} and 10^{-15} m^2 s^{-1}, respectively. Randomly re-arranging the microgels suggested that microgel distribution has no effect on chemokine gradients (Figure 4C,D), an important observation given the stochastic nature of microgel

encapsulation within hydrogel composites. Finally, we varied microgel diameter, keeping the density of microgels constant at 2.5 v/v%. The model, contrasting our ELISA data (Figure 3E), indicates that 50 µm microgels produce a steeper gradient compared to 150 µm microgels (Figure 4E,F).

2.5. Microgel-Delivered PDGF-BB Induces TPC Invasion into Composite Hydrogels

Given our in vitro and in silico observations that HepMA incorporation critically governs the rate of soluble factor release from hybrid microgels, we explored the effect of HepMA content on TPC recruitment in a novel, composite hydrogel that facilitates simultaneous control over topographical and soluble features of the microenvironment. Hybrid microgels (150 µm diameter) containing varying amounts of HepMA were loaded with PDGF-BB at 500 ng mL^{-1} and incorporated into hydrogels at 2.5 v/v%. To evaluate the effect of microgel-mediated, sustained delivery of PDGF-BB on spheroid outgrowth, we included a condition lacking microgels where soluble PDGF-BB was instead added directly to the media (10 ng mL^{-1}) immediately following encapsulation and again on day 2. These studies demonstrated that microgels containing 5 wt/v% HepMA result in more outgrowth compared to both the vehicle and soluble PDGF-BB groups (**Figure 5**A–E). To visualize the microgels and determine to what extent migrating cells physically interact with them, microgels were fluorescently labeled with fluorescein. High magnification imaging revealed that invading cells recruited and migrated along fiber segments, traveling around rather than on or through the microgels (Figure 5F). This observation was not surprising given that photo-crosslinked DexVS is not proteolytically cleavable, and microgels were not functionalized with cell-adhesive ligands. Considering the possibility that sequestration of cell-secreted factors[13a] is responsible for enhanced TPC recruitment relative to that elicited by soluble PDGF-BB (Figure 5B–E), we performed an additional experiment with non-loaded microgels and found that heparin content alone has no effect on TPC invasion (Figure S5A–D, Supporting Information). These results, in conjunction with our finding that TPC outgrowth is insensitive to PDGF-BB concentration (Figure 1B–E), strongly indicate that microscale, spatial organization of soluble factor presentation[29] is responsible for the observed enhancement in cell recruitment.

Future pre-clinical studies in rodents aiming to repair tendon injuries will require small volumes (≈3–5 µL) of hydrogel solution cross-linked in situ. The inclusion of smaller microgels would improve homogeneity of the injected material, with a more consistent number of microgels delivered upon injection. The ELISA and computational data differed on the effect of microgel size on soluble factor release profile (Figures 3E and 4F), and so we evaluated the effect of microgel size on spheroid outgrowth by incorporating 50 or 150 µm, PDGF-BB-laden microgels at 2.5 v/v%. Contrasting the computational model (Figure 4), we observed minimal differences in TPC invasion as a function of microgel size (Figure S5E–H, Supporting Information). A likely explanation for this disparity may be that the two microgel diameters result in unequal but sufficient PDGF-BB delivery to augment TPC outgrowth, especially

given that this outgrowth is stimulated over a range of non-zero concentrations when added directly to the media (Figure 1B–E).

A key benefit of this material system is its injectability. At minimum, as an adjunct to open surgical repair of an injured tendon, injectability (as compared to a pre-formed hydrogel graft) would allow the material to completely fill the intricate geometry of a tendon defect, maximizing the interface between the hydrogel and adjacent tissues to facilitate TPC recruitment and regeneration. For non-operative management following tendon rupture,[30] this material could be a delivered through a minimally invasive, transcutaneous injection at the site of the defect. Ultrasound guidance may be required in this case, but ultrasound-guided injections are already a clinical standard in the treatment of Achilles tendinopathy.[31] Despite the low viscosity of our material system prior to cross-linking, the inclusion of suspended fiber segments and microgels may complicate its injectability. Therefore, to demonstrate injectability of the composite system, we delivered a DexVS/VPMS gel mixture containing 2.5 v/v% each of fiber segments and 50 µm microgels through a 25-gauge needle into a mold with complex geometry, where it cross-linked to form a hydrogel (Figure S6, Supporting Information). Of note, confocal imaging of molded hydrogels showed no evidence of damage to either microgels or fibers or alterations to their random distribution following injection.

2.6. Microgel-Delivered PDGF-BB Drives TPC Recruitment from the Achilles Tendon

The physical and soluble cues studied above showed robust migratory responses in a TPC spheroid model, which was ideal for screening a wide parameter space given its high throughput and ease of assessment. However, utility of these cues requires validation in a more relevant model of cell recruitment from native tendon. Since previous studies have demonstrated a population of TPCs residing in the epitenon with tenogenic potential,[7g] we immunostained axial sections of adult (8–12 weeks) mouse AT and confirmed the presence of stem cell antigen (Sca)-1-positive progenitor cells in the epitenon (**Figure 6**A). We then established an ex vivo model of TPC recruitment from ATs explanted from adult Scleraxis (Scx)-GFP reporter mice. These genetically engineered mice were used to assess whether biomaterial-recruited TPCs possess tenogenic potential, as Scx is a well-established, early tenogenic transcription factor.[7e,f,32] Mouse ATs were halved at the midsubstance and encapsulated in fibrous (2.5 v/v% fiber density) hydrogel composites to study the effect of PDGF-BB delivered by 50 µm microgels containing 5 wt/v% HepMA (Figure 6B,C).

Progenitor cell recruitment during tendon healing in vivo is known to occur over the first 1–2 weeks following injury.[7b,c] To examine whether a different cell/tissue geometry influences microgel-generated PDGF-BB release over a relevant timeframe, we modified the COMSOL model to represent a 10x field of view adjacent to the surface of a mouse Achilles tendon explant and simulated release over a 10 day period. In contrast to the spheroid model, which produced a steady chemokine gradient over 3 days, the gradient in the tendon explant model demonstrated exponential decay over the 10 day period
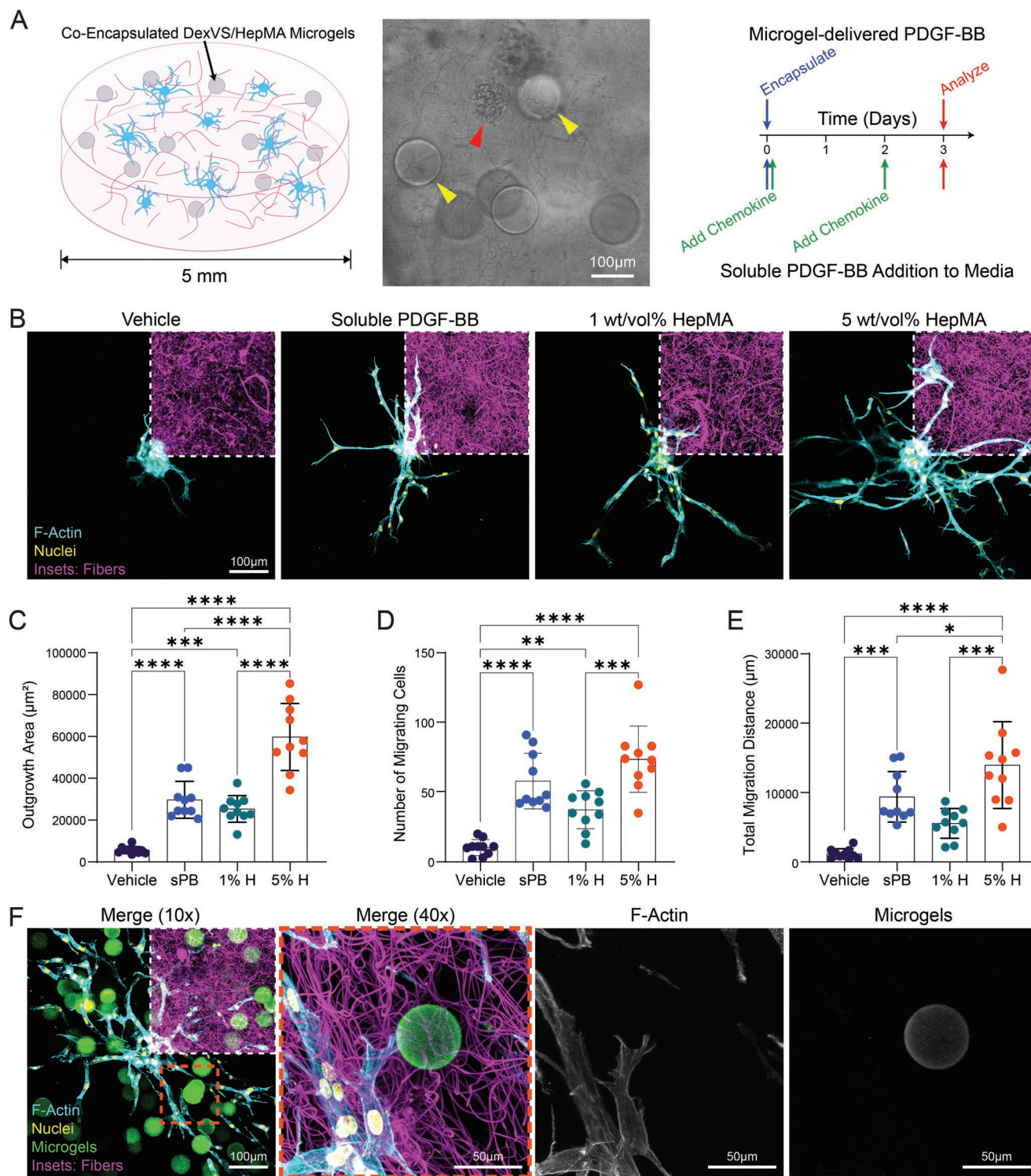
Figure 5. Microgel-delivered PDGF-BB drives 3D TPC invasion. A) Experimental schematic; brightfield image of spheroids (red arrowhead) and microgels (yellow arrowheads); timeline of cell encapsulation, chemokine addition for the soluble PDGF-BB condition, and fixation. B) Confocal fluorescent images of TPC outgrowth in response to basal media (Vehicle), soluble PDGF-BB (sPB), and PDGF-BB released from microgels containing 1 (1% H) or 5 (5% H) wt/v% HepMA. Quantification of C) TPC outgrowth area (μm^2), D) number of migrating cells, and E) total migration distance (μm) ($n = 10$, $N = 2$). F) TPC outgrowth in response to PDGF-BB released from fluorescein-labeled microgels (5 wt/v% HepMA); orange dotted line in the 10x merge (650 μm z-range) denotes region displayed in the 40x images (100 μm z-range). All data are presented as mean $\pm$ standard deviation. Asterisks indicate statistically significant comparisons, with $^*p < 0.05$, $^{**}p < 0.01$, $^{***}p < 0.001$, and $^{****}p < 0.0001$ by ordinary one-way ANOVA with Tukey's multiple comparisons test.
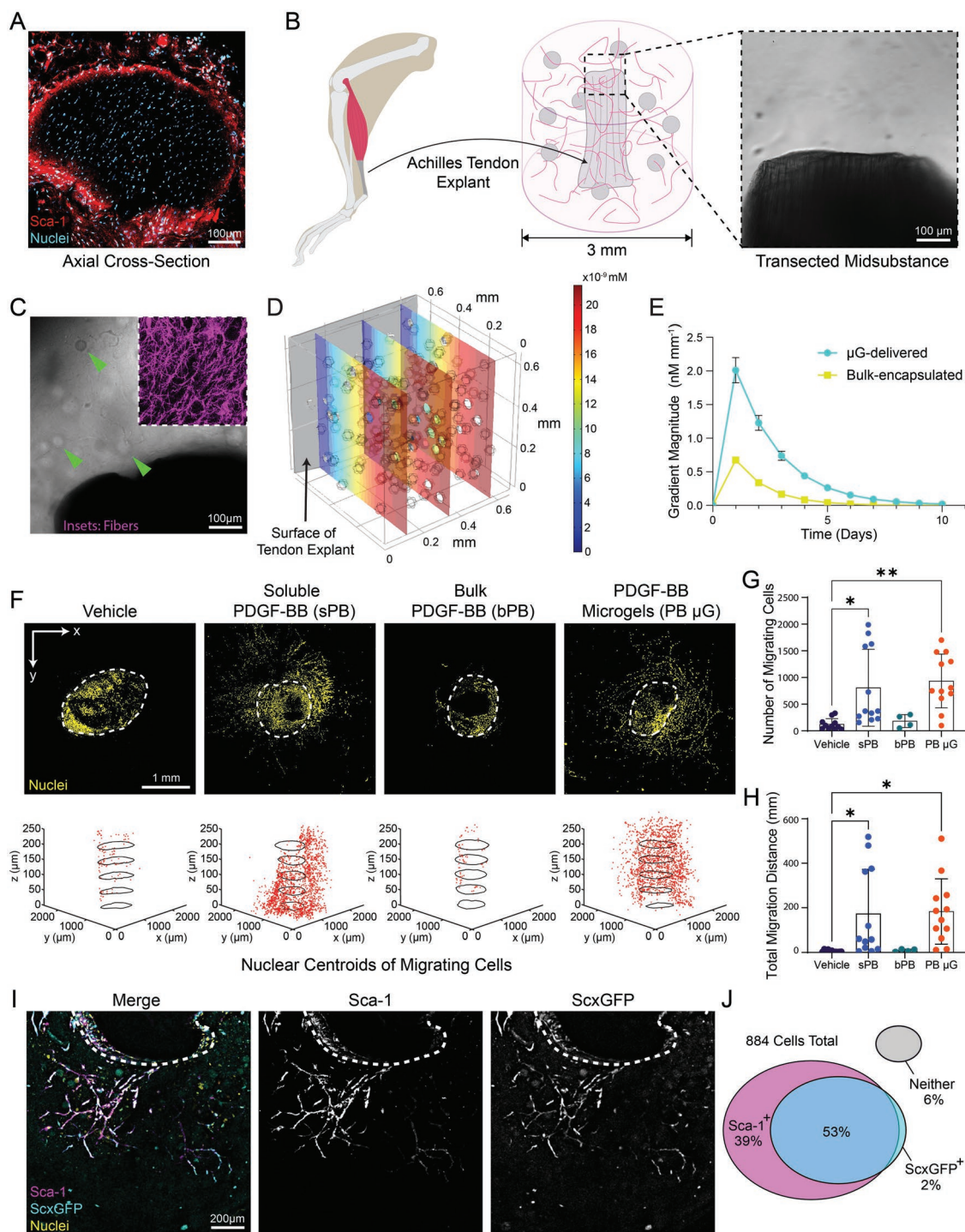
Figure 6. Microgel-delivered PDGF-BB recruits Scx+ TPCs from explanted murine Achilles tendon. A) Confocal fluorescent image of an axial cross section of a mouse AT demonstrating Sca-1+ progenitors residing in the epitenon. B) Experimental schematic; brightfield image of the transected tendon midsubstance encapsulated in a DexVS hydrogel. C) Brightfield image of an encapsulated tendon in a fibrous (inset) DexVS hydrogel containing hybrid microgels (green arrows). D) COMSOL model rendering of spatial distribution of PDGF-BB released from 50 μm microgels in the tendon explant model on day 10. E) Gradient of PDGF-BB concentration (nM mm^{-1}) over the first 20 microns adjacent to the tendon explant boundary for microgel-delivered versus bulk-encapsulated (12 ng mL^{-1}) PDGF-BB ($n = 5$ radial directions). F) Confocal fluorescent images (axial view) of cell nuclei within and migrating from the tendon, orthogonally projected over a 500 micron stack of images, where white dotted lines mark the tissue boundary; 3D plots of nuclear centroids (red dots) outside the tissue boundary (black contours) showing the first 250 μm of tissue adjacent to the transection site for simplicity. Quantification of G) number of migrating cells and H) total migration distance (μm) within 500 μm of the transection site ($n = 12$, $N = 3$ [$n = 4$ in bPB group]). I) Representative confocal fluorescent image of migrating ScxGFP reporter cells, stained for Sca-1 ($n = 5$, $N = 2$). J) Quantification of Sca-1 and ScxGFP positivity among migrating cells. All data are presented as mean ± standard deviation. Asterisks indicate statistically significant comparisons, with $^*p < 0.05$ and $^{**}p < 0.01$ by ordinary one-way ANOVA with Tukey's multiple comparisons test.

**ADVANCED
SCIENCE NEWS**

www.advancedsciencenews.com

**ADVANCED
FUNCTIONAL
MATERIALS**

www.afm-journal.de

(Figure 6D,E), likely stemming from a higher magnitude of flux into the tendon explant compared to that of the smaller cell spheroid. To isolate the effect of the microgels themselves, we evaluated a model containing no microgels but with the initial condition of a uniform distribution of PDGF-BB throughout the hydrogel. Even though the initial concentration of PDGF-BB was equal to the average initial concentration taken across the volume of the microgel model (12.5 ng mL^{-1}), microgel-mediated delivery yielded a more than threefold higher PDGF-BB gradient at all timepoints (Figure 6E).

Our findings in silico motivated four experimental conditions for the ex vivo model: 1) a vehicle control, 2) soluble PDGF-BB replenished in the media every 48 h (10 ng mL^{-1}), 3) PDGF-BB mixed into the hydrogel bulk prior to gelation at 12.5 ng mL^{-1} (same total input mass of PDGF-BB as in group 4), and 4) microgel-delivered PDGF-BB (loaded at 500 ng mL^{-1}, and incorporated at 2.5 v/v%). During healing, the majority of TPCs are likely recruited from the region of epitenon adjacent to the wound site,[7b–e] and so only the first 500 μm of tissue adjacent to the transection site was considered. This focused analysis also sought to maintain equivalence of proximal and distal segments. Over the course of 10 days, TPC invasion from explanted murine ATs was strongly encouraged by microgel-delivered PDGF-BB, on par with a condition where soluble PDGF-BB was replenished at 48 h intervals (Figure 6F–H; Figure S7 and Video S1, Supporting Information). In agreement with the computational model, an initial, uniform distribution of PDGF-BB resulted in minimal TPC outgrowth, similar to the vehicle control. However, in contrast to the 3 day spheroid outgrowth model, TPC recruitment in response to microgel-delivered PDGF-BB did not exceed that of the soluble PDGF-BB condition, implying that depletion of microgel payload over the 10 day period negated any beneficial effects garnered from spatially organized delivery.[29]

For invading TPCs to contribute productively to the repair process following tendon injury, at minimum, it is critical that they have the capacity to differentiate toward a tenogenic lineage.[7f] Use of AT explants from ScxGFP reporter mice[33] allowed us to evaluate whether tendon cells recruited into composite hydrogels maintained tenogenic potential. Staining for Sca-1 indicated that the majority of recruited cells were indeed multipotent progenitors, likely originating from the epitenon (Figure 6A,I). Moreover, a majority of these TPCs showed evidence of a pro-tenogenic phenotype as evidenced by ScxGFP expression (Figure 6I,J). While future work will focus on determining the salient microenvironmental features conducive to tenogenic differentiation, we suspect that the fibrous topography plays a major role by governing the spread state of TPCs. For example, in vitro chondrogenesis is favored in microenvironments that present minimal adhesive cues (e.g., alginate) such that the cells maintain a rounded morphology.[34] Indeed, cell shape is known to regulate lineage commitment in stem cells,[35] with previous work suggesting that a spindle morphology may bias stem cells toward a tenogenic lineage.[36]

3. Conclusion

Here, we developed a composite hydrogel system capable of delivering tunable mechanical, soluble, and topographical microenvironmental cues to recruit tendon progenitor cells across multiple in vitro settings. This system revealed that microgel-delivered PDGF-BB and fibrous topography potently drive TPC invasion into synthetic hydrogel matrices in both a TPC spheroid and ex vivo Achilles tendon model. Overall, this work suggests that modular, fiber-reinforced DexVS hydrogels offer a promising route toward a regenerative tendon scaffold given their: 1) mechanical durability evidenced by the range of bulk moduli permissive to fiber-mediated migration, and 2) programmed regulation of the soluble milieu following a single administration. Furthermore, given that this injectable, acellular material can be administered via a minimally invasive procedure and does not require patient or donor cell isolation,[37] it would face fewer regulatory hurdles and have lower associated costs. Finally, our evidence of tenogenic potential in invading TPCs motivates future work where we will leverage fibrous topographical alignment and timed growth factor delivery to orchestrate the spread state and organization of invading TPCs, tenogenic differentiation, alignment of de novo ECM, and ultimately, functional tissue regeneration.

4. Experimental Section

Cell Isolation and Culture: For all animal procedures, the Institutional Animal Care and Use Committee (IACUC) guidelines for survival surgery in rodents and the IACUC Policy on Analgesic Use in Animals Undergoing Surgery were followed (Protocol #PRO00009868). All cells used in this work were harvested from 6 to 9-week-old C57BL/6J mice (Jackson Laboratory, Bar Harbour, ME). Tail tendons were removed from euthanized mice and then encapsulated in 2 mg mL^{-1} type I collagen. Encapsulated tissues were cultured in an incubator set to 37 °C and 5% CO$_2$ in DMEM containing L-glutamine (Thermo Fisher, Waltham, MA), 1 v/v% penicillin/streptomycin/fungizone, and 10 v/v% fetal bovine serum (basal media) for 10 days to allow tendon progenitor cells (TPCs) to migrate into the collagen gel.[38] Following isolation and expansion of TPCs, collagen gels were digested in 0.25 mg mL^{-1} collagenase from *C. histolyticum* with 0.025 w/v% trypsin-EDTA. The resulting slurry was filtered through a cell strainer and then plated. Adherent TPCs were cultured in basal media, and cells at passage 1 were used for all experiments. For studies where cell proliferation was inhibited, TPC cultures were treated with 40 μg mL^{-1} mitomycin C for 2 h, washed with basal media, then incubated for at least 1 h prior to trypsinization for use in outgrowth studies.

Polymer Synthesis: Dextran functionalized with vinyl sulfone groups (DexVS) was synthesized as previously described.[39] Briefly, 5 g of 86 kDa dextran (MP Biomedicals, Irvine, CA) was dissolved in a 250 mL solution of 100 mm sodium hydroxide in Milli-Q water. On a stir plate set to 700 rpm, divinyl sulfone (Alfa Aesar, Haverhill, MA) was added to the solution, and the reaction proceeded for 3.5 min before termination by addition of 2.5 mL of 12 m hydrochloric acid. To achieve vinyl sulfone/dextran repeat unit ratios appropriate for hydrogel formation (16%) and fiber fabrication (65%), 3.88 and 12.5 mL of divinyl sulfone were added to substitution reactions, respectively. After vinyl sulfone addition, the product was dialyzed against Milli-Q water for 72 h with twice daily changes and then lyophilized for 72 h to yield a dry product. All reaction products were characterized via ^{1}H NMR.

Heparin methacrylate (HepMA) was synthesized as previously described.[26,40] Briefly, 0.5 g of 13.5–15 kDa heparin from porcine intestinal mucosa was dissolved in 50 mL of sterile PBS, and sodium hydroxide was added dropwise to bring the pH to 9. The solution was placed on a stir plate in a 4 °C refrigerator, then while stirring at

500 rpm, 99.3 µL of methacrylic anhydride was added. Sodium hydroxide was added intermittently over the next 24 h to maintain a pH of ≈8. The product was then dialyzed against Milli-Q water and lyophilized as described above.

Fiber Segment Fabrication and Functionalization: An electrospinning solution was prepared by dissolving DexVS (65% vinyl sulfone functionalization) in a 1:1 solution of dimethyl formamide and Milli-Q water with 0.015 wt/v% 2-Hydroxy-4′-(2-hydroxyethoxy)-2-methylpropiophenone (Irgacure 2959) photoinitiator. For fluorescent visualization of fibers, methacrylated rhodamine (Polysciences, Inc., Warrington, PA) was added at 0.5 mm. In a humidity-controlled glovebox (21 °C, 30–35% humidity), DexVS fibers were electrospun onto a slowly rotating (linear velocity 3.14 cm s^{-1}), grounded mandrel using a gap distance of 7 cm, voltage of −7.5 kV, and flow rate of 0.2 mL h^{-1}. An ultraviolet lamp was directed at the opposite side of the mandrel; every 15 min, the lamp was turned on for 5 min to expose deposited fibers to 100 mW cm^{-2} UV light. Continuous UV exposure over the course of layer-by-layer fiber deposition ensured that fibers were adequately and uniformly photo-crosslinked.

The cross-linked fiber mat was removed from the mandrel and transferred to Milli-Q water. Two rounds of pipetting, vortexing, centrifugation, and resuspension were performed to break up the fiber mat into individual fiber segments and remove any clumps and residual cross-linking reagents. Purified fibers were resuspended at 10 v/v% in PBS and stored in a light-protected box at 4 °C. Prior to use in hydrogel constructs, fiber segments were functionalized by resuspension in 50 mm 4-(2-hydroxyethyl)-1-piperazineethanesulfonic acid (HEPES) buffer at 10 v/v% along with cell-adhesive CGRGDS (RGD) (2.0 mm) and 5 mm sodium hydroxide. Functionalization proceeded via Michael-type addition at 37 °C for 15 min, then fibers were washed with PBS and resuspended in HEPES buffer.

Fabrication of Composite Hydrogels: DexVS hydrogels were formed using previously described methods.[10] Briefly, DexVS was dissolved in PBS containing 50 mm HEPES buffer. Either cell-adhesive RGD or scrambled CGRDGS (RDG) was incorporated at 2.0 mm. Additionally, to control the number of VS groups available for cross-linking, cysteine was added at 9.1 mm. After this pre-reaction proceeded on ice for 20 min, other components (functionalized fiber segments, microgels, spheroids, etc.) were added to the mixture followed by the addition of an MMP-cleavable, dithiolated GCRDVPMSMRGGDRCG (VPMS) cross-linking peptide. Gelation via Michael-type addition was initiated by addition of sodium hydroxide (33 mm) and carried out at 37 °C for 35 min before hydration in basal media. Bulk stiffnesses of ≈0.5 and 2.0 kPa were achieved by cross-linking DexVS hydrogels with 12.5 and 15.0 mm VPMS, respectively; DexVS concentrations of 3.3 and 3.4 wt/v% were used to ensure that the ratio of free vinyl sulfone groups to VPMS molecules was consistent between the two conditions.[10] To demonstrate injectability of the composite hydrogel, plain (only DexVS and VPMS) and composite (containing fibers and DexVS/HepMA microgels) hydrogel mixtures were loaded into a syringe and injected through a 25-gauge needle into polylactic acid molds with irregular geometries. Following cross-linking of the hydrogels, molds were dissolved in PBS overnight.

TPC Spheroid Formation and Encapsulation: TPC spheroids were formed by seeding 0.2 million cells on 400 µm Aggrewell plates (Stemcell Technologies, Vancouver, BC, Canada) coated with Pluronic F-127 followed by centrifugation at 400 g and overnight incubation. This seeding density yielded ≈165 cells per spheroid. Polydimethylsiloxane (PDMS) (Dow, Midland, MI) was prepared at a 1:10 cross-linker:base ratio and cast to form circular molds (5 mm diameter, 1.8 mm height). Molds were plasma etched, bonded to 18 mm glass coverslips, coated with a solution of 2 mg mL^{-1} porcine skin gelatin and dried in an 80 °C oven to subsequently release hydrogels from circular molds. Spheroids were collected from Aggrewell plates via repeated pipetting in basal media. The resulting suspension was centrifuged at 150 g for 30 s, and the supernatant was replaced with 50 mm HEPES buffer before addition to the hydrogel mixture at 750 spheroids mL^{-1}. Thirty five micro liters of spheroid/hydrogel suspension was added to each mold, yielding ≈25 spheroids per hydrogel (Figures 1,2,4). After hydrating in basal

media and incubating overnight, gels were released from the molds and cultured free-floating.

Hybrid Microgel Synthesis and Chemokine Loading: Hybrid microgels composed of DexVS and HepMA were generated on a custom-designed microfluidic droplet generating device. Devices were designed in AutoCAD, and a master mold was fabricated using a SU-8 negative photoresist (Kayaku, Westborough, MA). PDMS (1:10 cross-linker:base ratio) devices were replica cast from SU-8 masters, cleaned, and bonded to glass as described above (see TPC spheroid formation and encapsulation). An aqueous phase was prepared by dissolving DexVS (16% functionalization) and HepMA in PBS with 50 mm HEPES buffer, 0.5 mg mL^{-1} lithium phenyl-2,4,6-trimethylbenzoylphosphinate photoinitiator, and 2 v/v% N-vinylpyrrolidone. DexVS and HepMA concentrations were varied to study their effect on soluble factor release profiles.

An oil phase was prepared by adding 1.0 wt/v% perfluoropolyethylene (Ran Biotechnologies, Beverly, MA) to HFE-7500 (3 m, St. Paul, MN), a perfluorinated mineral oil. A syringe pump was used to flow the aqueous and oil phases through the microfluidic droplet generating device at 0.5 and 1.0 mL h^{-1}, respectively, to generate water-in-oil droplets with a high degree of monodispersity (Figure 3). The resulting emulsion traveled through Tygon tubing to a second PDMS microfluidic device consisting of a series of 200 µm wide channels in a 1 × 1 cm array. This array was exposed under a UV lamp at 100 mW cm^{-2} throughout the droplet generation process, with each microgel receiving ≈20 s of exposure at the flow rate stated above.

The emulsion was collected and then broken by the addition of PBS and 20 v/v% perfluorooctanol (PFO) (Alfa Aesar, Haverhill, MA). Oil and PFO were removed from collected microgels via centrifugation for 5 min at 1000 g, and washed microgels were stored in PBS containing 4 v/v% penicillin/streptomycin/fungizone. To measure microgel diameter, a suspension of microgels was flowed in a monolayer across a polystyrene surface. A video of this flow was recorded on a brightfield microscope, with frames collected every 5 s, and custom MATLAB code (MathWorks, Portola Valley, CA) identified and measured diameters of microgels in each frame. Recombinant murine PDGF-BB (Peprotech, Cranbury, NJ) was then added to a suspension of microgels in 0.1 wt/v% bovine serum albumin (250 and 500 ng mL^{-1} for release profile characterization and cell-based studies, respectively). This suspension was incubated for 2 days at 4 °C, then microgels were washed twice with PBS containing 50 mm HEPES buffer before incorporation into hydrogels at 2.5 v/v%.

Chemokine Release Characterization: Hybrid microgels were fabricated with varying amounts of DexVS and HepMA using droplet generator devices that yielded spherical microgels with 50 or 150 µm diameters. After loading with PDGF-BB at 250 ng mL^{-1} and washing, 50 µL of microgels was resuspended in 150 µL of PBS containing 0.1 wt/v% bovine serum albumin in a microcentrifuge tube. At each timepoint, tubes were shaken and centrifuged, then 35 µL of supernatant was removed, replaced with fresh supernatant, and stored at −80 °C for the remainder of the study. PDGF-BB concentration in each sample was measured via ELISA (DuoSet, R&D Systems, Minneapolis, MN) to calculate the fraction of theoretically loaded PDGF-BB that was released at each timepoint throughout the assay.

Computational Modeling of Microgel-Mediated Chemokine Delivery: COMSOL Multiphysics (COMSOL AB, Stockholm, Sweden) was used to quantify and visualize spatial distributions of PDGF-BB undergoing Fickian diffusion in a 665 × 665 × 665 µm volume of a DexVS hydrogel. Spheres representing hybrid microgels loaded with 500 ng mL^{-1} were distributed at 2.5 v/v% around a 100 µm sphere representing a cell spheroid. The fluid diffusion coefficient of the microgels was varied to simulate HepMA incorporation, and the effect of this parameter was explored over a range of bulk diffusion coefficients. Flux was permitted at all boundaries, and equations representing the boundary conditions assumed that flux into one face of the model would match flux out of the opposite face. Any PDGF that diffused into the spheroid was eliminated from the model to simulate cell receptor binding. The model was sampled at 24 h intervals for 3 days by measuring the PDGF-BB concentration along lines drawn in the positive and negative x, y, and z

directions ($n = 6$) and then calculating the slope of this concentration with respect to distance from the spheroid boundary over the first 20 μm.

A similar model was developed to simulate the ex vivo model, wherein the analyzed volume was the $665 \times 665 \times 665$ μm region adjacent a 1 mm diameter cylinder representing a mouse Achilles tendon. Similar to the cell spheroid, any PDGF-BB that diffused into the tendon was eliminated from the model. The model was sampled at 24 h intervals for 10 days in the form of PDGF-BB concentration along lines drawn normal to the tendon surface and ±25° in two orthogonal directions ($n = 5$). The slope of this concentration with respect to distance from the line's origin was then calculated over the first 20 μm.

Ex Vivo Achilles Tendon Outgrowth Model: Circular PDMS molds (4 mm diameter) were fabricated as above (Section 2.5), and a 0.5 mm thick PDMS ring with a 1.25 mm hole at the center was bonded at the base of each mold. Molds were coated with gelatin as above (Section 2.5). ATs were harvested from 9 to 12 week old C57BL/6 ScxGFP reporter mice.[33] Following euthanasia, hindlimbs were transected at the knee, skinned, and placed in a dish of Leibovitz's L-15 media (Thermo Fisher, Waltham, MA) containing 4 v/v% penicillin/streptomycin/fungizone and 10 v/v% fetal bovine serum. The AT was retrieved by making cuts at the myotendinous junction and calcaneal enthesis. Remaining fat and muscle tissue was then removed, and the tendon was transected at the midsubstance.

Tendons were washed in 25 μL of a DexVS hydrogel solution before being placed vertically in PDMS molds with the enthesis or myotendinous junction anchored by the ring at the base and the midsubstance facing upward. Twenty five micro liters of fibrous DexVS hydrogel solution was then transferred into each mold to encapsulate the tendons, and gels were hydrated with basal media after incubating for 35 min at 37 °C. After incubating overnight, gels were released from molds and cultured free-floating.

Microscopy and Image Analysis: Fluorescent images were captured on a Zeiss LSM800 confocal microscope. To quantify TPC spheroid outgrowth, samples were stained with phalloidin (Invitrogen, Waltham, MA) and Hoechst 33 342, and z-stacks were collected at 10x magnification and 5 μm intervals to encompass the volume of cell outgrowth for a given spheroid. Custom MATLAB code was developed to quantify outgrowth area as defined by F-actin-positive regions outside of the spheroid body in a max-projection of the imaged volume. This code also identified the 3D coordinates of centroid of nuclei outside the spheroid body, calculated their distance from the center of the spheroid body, and counted the number of migrating cells in addition to their total migration distance. For proliferation studies, cells were also stained with Ki67 (Ki67 rabbit anti-mouse, Invitrogen, Waltham, MA), and the number of Ki67+ nuclei was counted manually.

Encapsulated ATs treated with soluble PDGF-BB or PDGF-BB-laden microgels were stained with Hoechst 33 342 and an antibody against stem cell antigen (Sca)-1 (Sca-1 [Ly-6A/E] rat anti-mouse, Invitrogen, Waltham, MA). At 10x magnification, z-stacks of nuclei, immunostained Sca-1, and ScxGFP expression were collected at 5 μm intervals, spanning the first 500 μm of tendon adjacent to the transection site (midsubstance). Gaussian filters were applied to all images to remove noise and background. A custom MATLAB code demarcated the boundary of the tendon tissue at 50 μm intervals, identified the 3D coordinates of migrating nuclei, and quantified the intensity of the Sca-1 and ScxGFP channels in pixels contained in a $5 \times 5 \times 5$ μm cube centered at each nuclear centroid. Coordinates of nuclear centroids were also used to count the number of migrating cells and calculate their total migration distance from the nearest tissue boundary. For further visualization of cell recruitment, 3D renderings of TPC nuclei were generated in AVIA (AVIA Health, Chicago, IL).

Statistics: Pre-processing of all data involved exclusion of extreme outliers (i.e., greater than three interquartile ranges removed from the median). ELISA data from PDGF-BB release studies were also normalized to the theoretically loaded mass of PDGF-BB. All data were presented as mean ± standard deviation unless stated otherwise in the corresponding figure legend. Sample size was indicated within corresponding figure legends, with n technical replicates and N biological replicates ($N = 1$ unless stated otherwise). For ex vivo studies, each mouse yielded four samples, and so a total of 10 mice were used across three experiments ($N = 1$ for bulk PDGF-BB group). Statistical significance was determined by ordinary one- or two-way analysis of variance (ANOVA) with Tukey's multiple comparisons test or two-sided Student's t-test where appropriate ($\alpha = 0.05$). All statistical analyses were performed in Prism (GraphPad Software, San Diego, CA).

Supporting Information

Supporting Information is available from the Wiley Online Library or from the author.

Conflict of Interest

The authors declare no conflict of interest.

Authors Contribution

R.N.K., M.L.K., A.C.A., A.S., A.H, and B.M.B designed the experiments. A.C.A. developed the TPC isolation protocol. R.N.K, M.S., M.E.B., and A.S. contributed to in vitro and ex vivo outgrowth experiments and data analysis. E.P. built and analyzed the computational models. J.X. created images and videos of 3D renderings of cell nuclei for the ex vivo studies. D.L.M. and H.L.H electrospun and segmented DexVS fibers, and H.L.H formed TPC spheroids. W.Y.W contributed an in vitro cell migration platform for initial screening of TPC chemokines. R.N.K. adapted the microfluidic droplet generators from an original design by J.S., and S.J.D. fabricated them. R.N.K. and B.M.B. wrote the manuscript. All authors reviewed the manuscript.

Data Availability Statement

The data that support the findings of this study are available from the corresponding author upon reasonable request.

[1] United States Bone and Joint Initiative: The Burden of Musculoskeletal Disease in the United States, Fourth Edition, American Academy of Orthopedic Surgeons, **2016**.

[2] A. Praemer, S. Furner, D. P. Rice, *Musculoskeletal Conditions in the United States*, American Academy of Orthopedic Surgeons, IL, USA **1999**.

[3] N. J. Lemme, N. Y. Li, S. F. DeFroda, J. Kleiner, B. D. Owens, *Orthop J Sports Med* **2018**, *6*, 232596711880823.

[4] a) I. Lantto, J. Heikkinen, T. Flinkkila, P. Ohtonen, P. Siira, V. Laine, J. Leppilahti, *Am. J. Sports Med.* **2016**, *44*, 2406; b) K. Nilsson-Helander, K. G. Silbernagel, R. Thomee, E. Faxen, N. Olsson, B. I. Eriksson, J. Karlsson, *Am. J. Sports Med.* **2010**, *38*, 2186.

[5] a) M. L. Killian, L. Cavinatto, L. M. Galatz, S. Thomopoulos, *J Shoulder Elbow Surg* **2012**, *21*, 228; b) L. G. Józsa, P. Kannus, *Human Tendons: Anatomy, Physiology, and Pathology*, Human Kinetics, IL, Champaign **1997**.

[6] R. James, G. Kesturu, G. Balian, A. B. Chhabra, *J Hand Surg Am* **2008**, *33*, 102.

[7] a) M. E. Jones, V. Mudera, R. A. Brown, A. D. Cambrey, A. O. Grobbelaar, D. A. McGrouther, *J Hand Surg Am* **2003**, *28*, 221; b) F. Wu, M. Nerlich, D. Docheva, *EFORT Open Rev* **2017**, *2*, 332; c) P. Sharma, N. Maffulli, *J Musculoskelet Neuronal Interact* **2006**, *6*, 181; d) K. T. Best, A. Korcari, K. E. Mora, A. E. Nichols, S. N. Muscat, E. Knapp, M. R. Buckley, A. E. Loiselle, *Elife* **2021**, *10*, e; e) K. T. Best, A. E. Loiselle, *FASEB J.* **2019**, *33*, 8578; f) K. Howell, C. Chien, R. Bell, D. Laudier, S. F. Tufa, D. R. Keene, N. Andarawis-Puri, A. H. Huang, *Sci. Rep.* **2017**, *7*, 45238; g) T. Harvey, S. Flamenco, C. M. Fan, *Nat. Cell Biol.* **2019**, *21*, 1490.

[8] a) R. J. de Vos, A. Weir, H. T. van Schie, S. M. Bierma-Zeinstra, J. A. Verhaar, H. Weinans, J. L. Tol, *JAMA, J. Am. Med. Assoc.* **2010**, *303*, 144; b) S. Font Tellado, E. R. Balmayor, M. Van Griensven, *Adv. Drug Delivery Rev.* **2015**, *94*, 126; c) W. M. Efird, A. G. Fletcher, R. W. Draeger, J. T. Spang, L. E. Dahners, P. S. Weinhold, *Orthop J Sports Med* **2018**, *6*, 232596711880279; d) H. Tempfer, A. Kaser-Eichberger, C. Lehner, R. Gehwolf, S. Korntner, N. Kunkel, A. Wagner, M. Gruetz, L. M. Heindl, F. Schroedl, A. Traweger, *Cell. Physiol. Biochem.* **2018**, *46*, 1148; e) S. Tarafder, C. Ricupero, S. Minhas, R. J. Yu, A. D. Alex, C. H. Lee, *Theranostics* **2019**, *9*, 4241.

[9] a) S. Tarafder, J. A. Brito, S. Minhas, L. Effiong, S. Thomopoulos, C. H. Lee, *Biofabrication* **2019**, *12*, 015008; b) J. P. Yoon, C. H. Lee, J. W. Jung, H. J. Lee, Y. S. Lee, J. Y. Kim, G. Y. Park, J. H. Choi, S. W. Chung, *Am. J. Sports Med.* **2018**, *46*, 1441; c) F. Qu, J. L. Holloway, J. L. Esterhai, J. A. Burdick, R. L. Mauck, *Nat. Commun.* **2017**, *8*, 1780; d) Y. Wang, S. Jin, D. Luo, D. He, C. Shi, L. Zhu, B. Guan, Z. Li, T. Zhang, Y. Zhou, C. Y. Wang, Y. Liu, *Nat. Commun.* **2021**, *12*, 1293; e) A. English, A. Azeem, K. Spanoudes, E. Jones, B. Tripathi, N. Basu, K. McNamara, S. A. M. Tofail, N. Rooney, G. Riley, A. O'Riordan, G. Cross, D. Hutmacher, M. Biggs, A. Pandit, D. I. Zeugolis, *Acta Biomater* **2015**, *27*, 3.

[10] D. L. Matera, W. Y. Wang, M. R. Smith, A. Shikanov, B. M. Baker, *ACS Biomat. Sci. Eng.* **2019**, *5*, 2965.

[11] a) A. M. Tatara, A. G. Mikos, *J. Bone Joint Surg. Am.* **2016**, *98*, 1132; b) Y. J. No, M. Castilho, Y. Ramaswamy, H. Zreiqat, *Adv. Mater.* **2020**, *32*, 1904511.

[12] B. M. Baker, R. L. Mauck, *Biomaterials* **2007**, *28*, 1967.

[13] a) M. H. Hettiaratchi, T. Miller, J. S. Temenoff, R. E. Guldberg, T. C. McDevitt, *Biomaterials* **2014**, *35*, 7228; b) M. H. Hettiaratchi, M. S. Shoichet, *Tissue Eng Part A* **2019**, *25*, 925; c) T. E. Rinker, B. D. Philbrick, M. H. Hettiaratchi, D. M. Smalley, T. C. McDevitt, J. S. Temenoff, *Acta Biomater.* **2018**, *68*, 125; d) J. A. Zimmermann, M. H. Hettiaratchi, T. C. McDevitt, *Stem Cells Transl Med* **2017**, *6*, 223.

[14] a) H. L. Hiraki, D. L. Matera, M. J. Rose, R. N. Kent, C. W. Todd, M. E. Stout, A. E. Wank, M. C. Schiavone, S. J. DePalma, A. A. Zarouk, B. M. Baker, *Front Bioeng Biotechnol* **2021**, *9*, 679165; b) D. L. Matera, A. T. Lee, H. L. Hiraki, B. M. Baker, *Cell Mol. Bioeng.* **2021**, *14*, 381; c) M. Vinci, C. Box, S. A. Eccles, *J. Vis. Exp.* **2015**, https://doi.org/10.3791/52686e52686; d) Y. C. Huang, T. J. Liu, *Acta. Biomater.* **2012**, *8*, 1048.

[15] a) K. B. Sugg, J. F. Markworth, N. P. Disser, A. M. Rizzi, J. R. Talarek, D. C. Sarver, S. V. Brooks, C. L. Mendias, *Am. J. Physiol. Cell Physiol.* **2018**, *314*, C389; b) D. A. Kaji, K. L. Howell, Z. Balic, D. Hubmacher, A. H. Huang, *Elife* **2020**, *9*.

[16] Y. Lim, M. Lee, H. Jeong, H. Kim, *Dev. Reprod.* **2017**, *21*, 167.

[17] a) J. G. Tidball, M. J. Spencer, *J. Cell Biol.* **1993**, *123*, 627; b) K. Mellstrom, C. H. Heldin, B. Westermark, *Exp. Cell Res.* **1988**, *177*, 347.

[18] a) H. Seppa, G. Grotendorst, S. Seppa, E. Schiffmann, G. R. Martin, *J. Cell Biol.* **1982**, *92*, 584; b) B. H. Cochran, A. C. Reffel, C. D. Stiles, *Cell* **1983**, *33*, 939; c) K. E. Bornfeldt, E. W. Raines, L. M. Graves, M. P. Skinner, E. G. Krebs, R. Ross, *Ann. N. Y. Acad. Sci.* **1995**, *766*, 416.

[19] W. Y. Wang, D. Lin, E. H. Jarman, W. J. Polacheck, B. M. Baker, *Lab Chip* **2020**, *20*, 1153.

[20] D. L. Matera, K. M. DiLillo, M. R. Smith, C. D. Davidson, R. Parikh, M. Said, C. A. Wilke, I. M. Lombaert, K. B. Arnold, B. B. Moore, B. M. Baker, *Sci. Adv.* **2020**, *6*.

[21] a) B. M. Baker, R. P. Shah, A. M. Silverstein, J. L. Esterhai, J. A. Burdick, R. L. Mauck, *Proc. Natl. Acad. Sci. USA* **2012**, *109*, 14176; b) B. Trappmann, B. M. Baker, W. J. Polacheck, C. K. Choi, J. A. Burdick, C. S. Chen, *Nat. Commun.* **2017**, *8*, 371.

[22] G. Thrivikraman, A. Jagiello, V. K. Lai, S. L. Johnson, M. Keating, A. Nelson, B. Schultz, C. M. Wang, A. J. Levine, E. L. Botvinick, R. T. Tranquillo, *Proc. Natl. Acad. Sci. USA* **2021**, *118*.

[23] a) P. L. Ritger, N. A. Peppas, *J. Controlled Release.* **1987**, *5*, 23; b) P. L. Ritger, N. A. Peppas, *J. Controlled Release.* **1987**, *5*, 37.

[24] a) S. Utech, R. Prodanovic, A. S. Mao, R. Ostafe, D. J. Mooney, D. A. Weitz, *Adv. Healthcare Mater.* **2015**, *4*, 1628; b) A. G. Hati, D. C. Bassett, J. M. Ribe, P. Sikorski, D. A. Weitz, B. T. Stokke, *Lab Chip* **2016**, *16*, 3718; c) A. S. Mao, J. W. Shin, S. Utech, H. Wang, O. Uzun, W. Li, M. Cooper, Y. Hu, L. Zhang, D. A. Weitz, D. J. Mooney, *Nat. Mater.* **2017**, *16*, 236.

[25] a) R. Subbiah, A. Cheng, M. A. Ruehle, M. H. Hettiaratchi, L. E. Bertassoni, R. E. Guldberg, *Acta Biomater* **2020**, *114*, 63; b) S. E. Sakiyama-Elbert, J. A. Hubbell, *J. Controlled Release* **2000**, *65*, 389.

[26] C. D. Davidson, D. K. P. Jayco, D. L. Matera, S. J. DePalma, H. L. Hiraki, W. Y. Wang, B. M. Baker, *Acta Biomater* **2020**, *105*, 78.

[27] a) B. Mohanraj, G. Duan, A. Peredo, M. Kim, F. Tu, D. Lee, G. R. Dodge, R. L. Mauck, *Adv. Funct. Mater.* **2019**, *29*; b) L. C. Ionescu, G. C. Lee, B. J. Sennett, J. A. Burdick, R. L. Mauck, *Biomaterials* **2010**, *31*, 4113; c) M. N. Singh, K. S. Hemant, M. Ram, H. G. Shivakumar, *Res Pharm Sci* **2010**, *5*, 65; d) C. Y. Wong, H. Al-Salami, C. R. Dass, *Int. J. Pharm.* **2018**, *537*, 223; e) S. S. Datta, A. Abbaspourrad, E. Amstad, J. Fan, S. H. Kim, M. Romanowsky, H. C. Shum, B. Sun, A. S. Utada, M. Windbergs, S. Zhou, D. A. Weitz, *Adv. Mater.* **2014**, *26*, 2205.

[28] W. Y. Wang, R. N. Kent, S. A. Huang, E. H. Jarman, E. H. Shikanov, C. D. Davidson, H. L. Hiraki, D. Lin, M. A. Wall, D. L. Matera, J. W. Shin, W. J. Polacheck, A. Shikanov, B. M. Baker, *Acta Biomater* **2021**, *135*, 260.

[29] L. Pruett, C. Jenkins, N. Singh, K. Catallo, D. Griffin, *Adv. Funct. Mater.* **2021**, *31*.

[30] A. Soroceanu, F. Sidhwa, S. Aarabi, A. Kaufman, M. Glazebrook, *J. Bone Joint Surg. Am.* **2012**, *94*, 2136.

[31] E. E. Drakonaki, G. M. Allen, R. Watura, *Br. J. Radiol.* **2016**, *89*, 20150577.

[32] a) A. H. Huang, H. H. Lu, R. Schweitzer, *J Orthop Res* **2015**, *33*, 800; b) T. Sakabe, K. Sakai, T. Maeda, A. Sunaga, N. Furuta, R. Schweitzer, T. Sasaki, T. Sakai, *J. Biol. Chem.* **2018**, *293*, 5766.

**ADVANCED
SCIENCE NEWS**

www.advancedsciencenews.com

**ADVANCED
FUNCTIONAL
MATERIALS**

www.afm-journal.de

[33] B. A. Pryce, A. E. Brent, N. D. Murchison, C. J. Tabin, R. Schweitzer, *Dev. Dyn.* **2007**, *236*, 1677.

[34] X. T. Mo, S. C. Guo, H. Q. Xie, L. Deng, W. Zhi, Z. Xiang, X. Q. Li, Z. M. Yang, *Bone* **2009**, *45*, 42.

[35] R. McBeath, D. M. Pirone, C. M. Nelson, K. Bhadriraju, C. S. Chen, *Dev. Cell* **2004**, *6*, 483.

[36] V. Kishore, W. Bullock, X. Sun, W. S. Van Dyke, O. Akkus, *Biomaterials* **2012**, *33*, 2137.

[37] M. Ni, Y. F. Rui, Q. Tan, Y. Liu, L. L. Xu, K. M. Chan, Y. Wang, G. Li, *Biomaterials* **2013**, *34*, 2024.

[38] A. Shimada, S. Wada, K. Inoue, H. Ideno, T. Kamiunten, K. Komatsu, A. Kudo, Y. Nakamura, T. Sato, K. Nakashima, A. Nifuji, *Histochem. Cell Biol.* **2014**, *142*, 205.

[39] Y. Yu, Y. Chau, *Biomacromolecules* **2012**, *13*, 937.

[40] S. J. DePalma, C. D. Davidson, A. E. Stis, A. S. Helms, B. M. Baker, *Biomater. Sci.* **2021**, *9*, 93.

2207556 (14 of 14)